E 6254

NASA Technical Memorandum 104420

A Three-Dimensional Navier-Stokes Stage Analysis of the Flow Through a Compact Radial Turbine

James D. Heidmann
Lewis Research Center
Cleveland, Ohio

NASA

A THREE-DIMENSIONAL NAVIER-STOKES STAGE ANALYSIS
OF THE FLOW THROUGH A COMPACT RADIAL TURBINE

James D. Heidmann
NASA Lewis Research Center
Cleveland, Ohio

Abstract

A steady, three-dimensional Navier-Stokes "average passage" computer code is used to analyze the flow through a compact radial turbine stage. The code is based upon the average passage set of equations for turbomachinery, whereby the flow fields for all passages in a given blade row are assumed to be identical while retaining their three-dimensionality. A stage solution is achieved by alternating between stator and rotor calculations, while coupling the two solutions by means of a set of axisymmetric body forces which model the absent blade row. Results from the stage calculation are compared with experimental data and with results from an isolated rotor solution having axisymmetric inlet flow quantities upstream of the vacated stator space. Although the mass-averaged loss through the rotor is comparable for both solutions, the details of the loss distribution differ due to stator effects. The stage calculation predicts smaller spanwise variations in efficiency, in closer agreement with the data. The results of this study indicate that stage analyses such as this hold promise for improved prediction of loss mechanisms in multi-blade row turbomachinery, which could lead to improved designs through the reduction of these losses.

Introduction

Radial-inflow turbines have many uses in the aircraft and power generation industries. For a given work factor (specific work divided by blade speed squared), a radial turbine stage will generally have a higher efficiency than a small axial turbine. There are several reasons for this. First, a single stage radial turbine can expand the flow across a relatively large pressure ratio compared to an axial turbine stage. Thus a single stage radial turbine might be used where a multi-stage axial turbine would otherwise be required, reducing losses associated with a large number of blade rows. Secondly and more fundamentally, the reduction in radius occurring in a radial turbine flow permits a lower rotor exit velocity for the same expansion process, reducing fluid friction losses. The use of radial turbines for propulsion engines, although desirable from a performance standpoint, is nonetheless limited by their relatively large diameter and weight. In response to these limitations, Pratt and Whitney has designed and fabricated two compact radial turbine rotors which are compatible with turboshaft engines in the 1600 kilowatt class. The rotors are up to 50% shorter in axial length, 4% smaller in diameter, and 30% lighter than current state-of-the-art radial turbine rotors. These size reductions were realized through the application of advanced three-dimensional inviscid and viscous design codes. The rotors were tested in the Warm Turbine Test Facility at NASA Lewis Research Center.

A three-dimensional Navier-Stokes analysis of the compact radial turbine stage was undertaken at NASA Lewis Research Center. The scope of this study is limited to the first of the two rotors designed and fabricated by Pratt and Whitney. The main goal of this analysis is to gain insight into the complex three-dimensional flow in the compact radial turbine stage by modeling the flow in this high-speed turbine stage as accurately as possible. Comparisons with experimental data and explanation of experimental trends aid in accomplishing this goal. A three-dimensional code is necessary for this analysis to adequately capture the three-dimensional secondary flows which produce and distribute loss in the turbine. This is consistent with the rationale for designing and optimizing the rotors using three-dimensional design codes.

Choo and Civinskas [1] analyzed a radial turbine flow using the three-dimensional inviscid DENTON code [2], and compared the results with limited experimental data. Trailing edge boundary layer separation and wake development were cited as possible causes of predicted underturning relative to experimental exit flow angles. Zangeneh-Kazemi et al. [3] conducted three-dimensional viscous analyses of a radial turbine with and without a tip clearance model, and compared the results with experimental data. Computed results agreed well with experimental data, particularly for the tip clearance case. It was thus concluded that a tip clearance model be incorporated for accurate simulation of radial turbine flow fields. Heidmann and Beach [4] presented a three-dimensional Navier-Stokes analysis of the compact radial turbine rotor of this study using an inviscid model, a viscous model with no clearance, and a viscous model with clearance. Reasonable agreement with experimental data was attained for the third model. In addition to these radial turbine analyses, several computational studies of centrifugal compressors have been reported. Moore and Moore [5] reported a three-dimensional viscous analysis for a centrifugal impeller using a steady partially-parabolic model. Results showed good agreement with data, except for some wake anomalies associated with leading edge effects beyond the scope of the model. Rhie et al. [6] also reported a three-dimensional viscous analysis of a centrifugal impeller using a partially-parabolic model. The importance of using a tip clearance model to accurately predict the wake flow was demonstrated.

The preceding studies were limited to analysis of an isolated rotating blade row, either a turbine or a compressor. Recently, substantial effort has been focused on accounting for multi-blade row turbomachine effects. Dawes [7] reported development of a viscous multistage analysis technique based on circumferential averaging of flow variables at inter-blade row mixing planes, while retaining radial variations. Improved comparison with experimental data relative to an isolated blade row calculation was reported for two cases. Denton [8] reported a procedure which also uses inter-blade row mixing planes to transfer information between adjacent blade rows, but allows flow quantities to vary circumferentially at the mixing plane to avoid errors associated with mixing planes very close to blade leading and trailing edges. The procedure is in early stages of development, and uses very sparse grids.

This paper presents a three-dimensional Navier-Stokes analysis of the flow through the compact radial turbine stage using the "average passage" code of Adamczyk [9-11]. This code models the flow as spatially periodic from blade passage to blade passage in a particular blade row and can be used to analyze interacting blade rows, including multistage machines. This becomes advantageous for multistage turbomachinery calculations involving stator and/or rotor blade rows having different blade count, where the averaging process keeps computational time from becoming prohibitive. For a single stage machine, the actual flow is identical for all passages in a particular blade row, so this averaging process has no effect. Tip and hub clearance models are included in the analysis, as recommended by Zangeneh-Kazemi et al. and Rhie et al. The hub clearance model is necessary to model the backface clearance found in this and other radial turbine rotors.

Turbine Description

The compact radial turbine stator is shown in Fig. 1. The stator consists of 36 blades which have an exit blade angle of approximately 73 degrees from the radial direction. The compact radial turbine rotor is shown in Fig. 2. The rotor consists of 14 solid blades and a solid disk. The stator and rotor blade leading and trailing edges are elliptic to reduce discontinuities in surface curvature. The flow enters the rotor radially and exits axially. As is typical for radial-inflow turbines, the rotor is scalloped to save weight and minimize centrifugal disk stresses. This means that the rotor disk surface does not extend completely to the blade leading edge. Instead, the flow is bounded by the stationary backface in this region. Nor does the disk surface extend substantially beyond the blade trailing edge. The hub surface is stationary upstream and downstream of the disk surface. Scalloping of the rotor also causes a clearance flow in the radial portion of the rotor hub, in addition to the familiar tip clearance. Figure 3 shows the stage assembly, indicating both clearances. Clearances were measured during operation. The shroud clearance was about 0.46 mm (0.018 in) at the leading edge and 0.20 mm (0.008 in) at the trailing edge. The backface clearance was about 0.38 mm (0.015 in). The rotor hub-to-shroud span was 14.12 mm (0.556 in) at the leading edge, and 44.00 mm (1.732 in) at the trailing edge. The leading edge hub and shroud clearances thus accounted for 2.69% and 3.26% of the leading edge span, respectively, for a total clearance of 5.95%. The trailing edge shroud clearance accounted for 0.45% of the trailing edge span. The rotor diameter was 0.367 m (14.46 in) to the blade leading edge. The stator blade outer and inner diameters were 0.449 m (17.66 in), and 0.386 m (15.20 in), respectively. The radial distance between blade rows in the vaneless space was 9.46 mm (0.372 in). Although the stator trailing edge span (b-width) was 12.40 mm (0.488 in), the inter-blade row shroud and actuator ring reduced the span to 11.91 mm (0.469 in) between blade rows. These dimensions reflect the scaled up experimental rig geometry.

The experimental study of the compact radial turbine was conducted in the NASA Lewis Research Center Warm Turbine Test Facility under a joint program with Pratt and Whitney [12,13]. Testing was conducted over a matrix of test conditions at reduced temperatures and pressures. The matrix consisted of a range of pressure ratios and rotor speeds centered about the design point. The nominal design point test conditions were 19,940 RPM, 5.03 total pressure ratio, 2.86 kg/s (6.30 lb/s) flow rate, 335 KPa (48.6 psi) inlet total pressure, and 479 K (863 R) total inlet temperature. This corresponds to a Reynolds number of 6.00×10^5 based on rotor leading edge diameter, mass flow rate, and stator inlet conditions. The fuel-to-air ratio for the experiment was 0.0042, yielding a gas constant of 288.1 m^2/s^2 K (1723 ft^2/s^2 R). The mean value of specific heat ratio was approximately 1.39. After completing testing on the first turbine configuration, the stator blades were rotated closed by 1.125 degrees to increase the swirl into the rotor and possibly improve the performance of the turbine. Tests of this second configuration, however, indicated a reduction in efficiency. A second rotor, even smaller than the first, was also designed and fabricated by Pratt and Whitney and tested at NASA Lewis Research Center. This third turbine configuration attained an efficiency comparable to that of the original turbine configuration when corrected for its higher work factor. The first and third configurations attained efficiencies approximately 2 percent higher than current state-of-the-art turbines of like work factor. The analysis of this paper is based on the first turbine configuration.
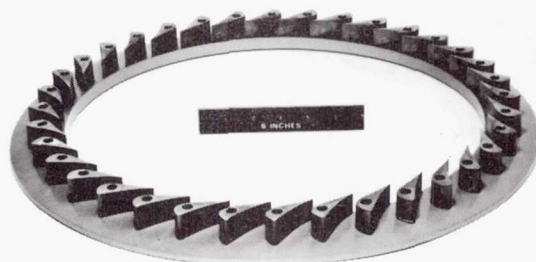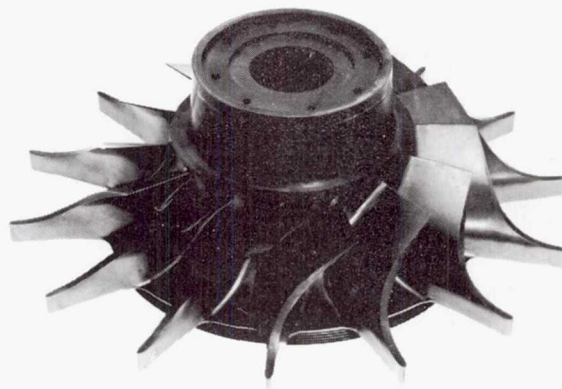

Figure 1. Stator ring

Figure 2. Compact radial turbine rotor

FLOW

STATOR BLADE

BACKFACE CLEARANCE

SHROUD CLEARANCE
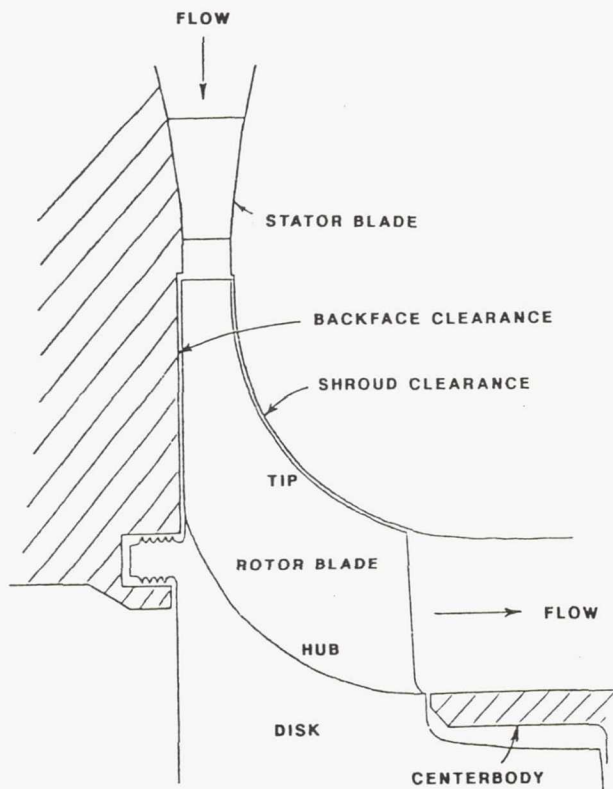
TIP

ROTOR BLADE

FLOW

HUB

DISK

CENTERBODY

Figure 3. Stage assembly

In addition to overall performance measurements, rotor exit surveys were conducted for each configuration which measured axisymmetric flow angles, total temperatures, and total pressures versus percent span. Although stator exit surveys were not conducted for the first turbine configuration, they were conducted for the second configuration, enabling limited comparison. All data were recorded at a steady-state condition. The design point data from these experiments are used for comparison to the average passage code calculations in this report.

Code Description

As stated earlier, the flow through the compact radial turbine was analyzed using a steady three-dimensional Navier-Stokes "average passage" code. The equations which form the basis for the average passage code are obtained by applying three averaging processes to the full Navier-Stokes equations. These processes are ensemble averaging, time averaging, and passage-to-passage averaging. Ensemble averaging yields the familiar Reynolds-averaged Navier-Stokes equations. This averaging process removes the random fluctuations from the flow field while retaining the unsteady deterministic fluctuations. Time averaging further simplifies the flow equations by removing the deterministic unsteady flow fluctuations. In multi-blade row turbomachinery, these are produced by the relative motion of stator and rotor blade rows. Passage-to-passage averaging removes differences between the flow fields in different blade passages of the same blade row, resulting in spatial periodicity in a particular blade row. For a single stage turbomachine subjected to axisymmetric boundary conditions (such as the turbine of this study), the first two averaging processes alone produce spatial periodicity. Thus the passage-to-passage averaging is redundant. For multistage turbomachinery with stator

blade rows having different numbers of blades and/or rotor blade rows having different numbers of blades, however, this will not generally be true. The average passage equations obtained by the three averaging processes are discretized using a control volume approach in a cylindrical coordinate system. Using this control volume approach, all flow quantities are cell-centered. To obtain values of flow variables at cell surfaces, a second-order accurate averaging process is used. A Baldwin-Lomax turbulence model is employed with a turbulent Prandtl number of 0.9, and is updated after every 10 iterations. Transition to turbulent flow is assumed to occur at 10% of the radial chord in the stator. The rotor is fully turbulent. A constant value of specific heat ratio is assumed in the code.

The discretized average passage equations obtained by the control volume approach are solved using a four-stage Runge-Kutta scheme. Second and fourth difference dissipation terms are used to avoid alternate point decoupling in the solution. The model of Jameson et al. [14] is used. The level of dissipation used is minimized to avoid excessive smoothing of the solution. Total temperature, total pressure, and axial and tangential velocities are specified at the upstream boundary. The Riemann invariants C^+ and C^- are used to calculate the radial velocity, static temperature, static pressure, and density at the upstream boundary. At the downstream boundary, the static pressure at the hub is specified and spanwise equilibrium is enforced. All other downstream flow quantities are extrapolated from the interior of the flow domain. At the blade, hub, and shroud surfaces, extrapolated normal pressure gradient and adiabatic wall boundary conditions are employed. These solid surfaces are modeled as no-slip and impermeable. For computational cells on the stationary shroud, backface, and aft centerbody surfaces, the no-slip condition results in rotation relative to the rotor. The mesh boundaries extending from the blade leading and trailing edges to the inflow and outflow boundaries, respectively, are periodic boundaries. At these boundaries, periodicity is enforced by setting the flow variables in the computational cell outside the computational domain equal to those at the corresponding periodic location. These periodic boundary conditions are also implemented in the clearance gap region. A simple one-dimensional inviscid flow model is used for the clearance gap flow. Mass, momentum, and total enthalpy are conserved across the clearance gap between adjacent grid points, resulting in zero static pressure difference across the gap. Although this model of the flow in the clearance region is quite simple, it does result in a flow across the clearance gap. This was found to be important for viscous flows in the previous study [4] due to the viscous drag of the shroud near the clearance region. If flow is not allowed to pass above the blade tip, the shroud boundary layer flow unrealistically stagnates at the blade.

Grid Generation

A three-dimensional computational grid was generated for the stator and rotor blade passages using an interactive H-grid generation procedure [15]. The procedure makes use of a combination algebraic/elliptic technique. For a multi-blade row calculation using the average passage code, it is necessary to produce a complete three-dimensional grid for each blade row, each of which spans the length of the computational domain in the meridional direction. Thus both a stator and a rotor grid were generated. Both grids extend the entire distance from the inlet flow boundary upstream of the stator to the exit flow boundary downstream of the rotor.

Periodic boundary surfaces extend from the leading and trailing edges of the blades to the inlet and exit bounaries, respectively. The inlet flow boundary is at a diameter of 0.534 m (21.04 in), more than one stator radial chord upstream of the stator leading edge. The exit flow boundary is located at the exit survey plane used in the experiment, approximately 2.5 rotor exit span lengths downstream of the rotor trailing edge. An axisymmetric two-dimensional grid (Fig. 4) is common to both the stator and the rotor grid. The three-dimensional grids are not axisymmetric, but the radial and axial coordinates of each grid point on the blade and periodic boundary surfaces of the three-dimensional grids are identical to those from the axisymmetric grid. Figures 5 and 6 show the midspan stator and rotor grids respectively. The stator and rotor grids consist of 173 by 37 by 37 grid points, with 173 grid points in the meridional direction. These are the only grids used in the calculation, so grid independence cannot be proven. However, with over 200,000 grid points in each grid, substantial increases in the number of grid points is impractical. There are 37 meridional grid points on the stator and 69 on the rotor. The hub and shroud clearance gaps contain 4 computational cells each in the spanwise direction. While this discretization of the clearance gaps approximates the magnitude of the actual machine clearance, it does not exactly duplicate the distribution of the clearance. However, since a very simple model is used in the clearance calculation, it was decided not to undermine the smoothness of the grid by exactly following the blade tip with a grid line. The computational shroud clearance varies from 0.21 mm (0.008 in) at the leading edge to 0.71 mm (0.028 in) at midchord to 0.27 mm (0.011 in) at the trailing edge. The computational hub clearance increases from 0.21 mm (0.008 in) at the leading edge to 0.51 mm (0.020 in) at the end of the clearance. When measured after disassembly of the experiment, the vaneless space span was found to be less than either the stator trailing edge or rotor leading edge spans. Since it was considered important to match the minimum span in this transonic region of the flow, the grid smoothly reaches the same minimum span. In the actual assembly, the hub and shroud contours change in a stepwise manner (see Figs. 3 and 4).
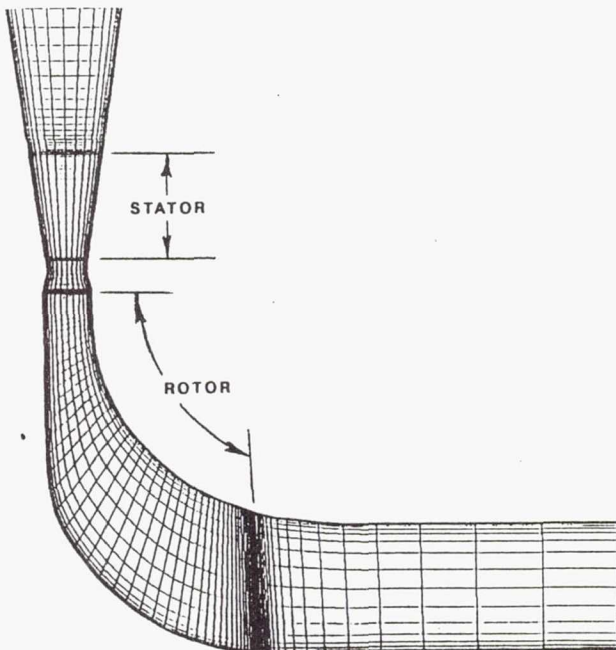

Figure 5. Stator midspan grid
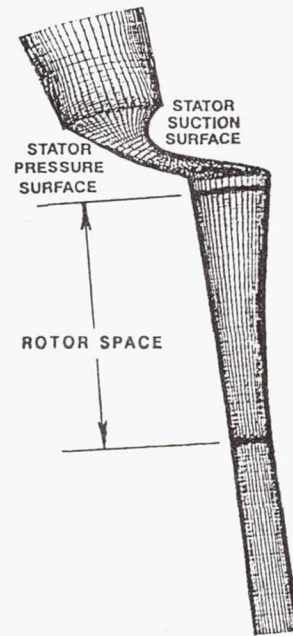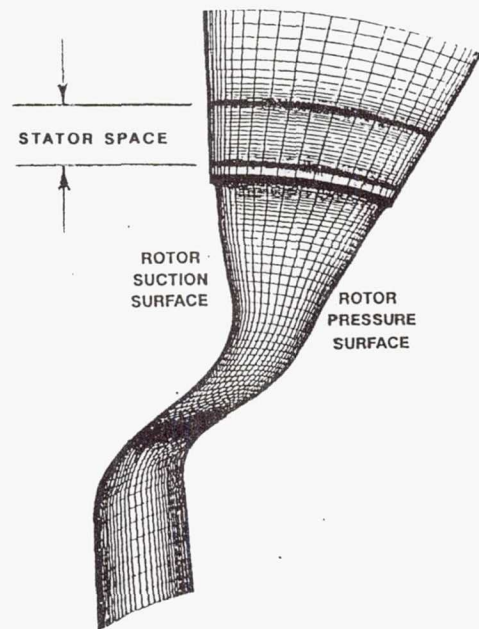

Figure 6. Rotor midspan grid

Figure 4. Axisymmetric grid

Grid points are densely packed near solid boundaries to adequately resolve viscous effects. The grid points are distributed in the blade-to-blade direction using the hyperbolic tangent function and in the spanwise direction using the exponential function. Grid points are also packed near the rotor leading and trailing edges and the stator trailing edge because of the large accelerations typically found in these regions. This clustering is done using the hyperbolic tangent function. The stator leading edge is thick and is exposed to low velocities, so clustering is not as important there. A sufficient

number of grid points lie on the leading and trailing edges of the stator and rotor blades to adequately describe the elliptic geometry. This is important because accelerations around leading and trailing edges are particularly sensitive to geometry. The grid spacing at the wall is less than about 0.12 mm (0.005 in) over the blade, hub, and shroud surfaces. This corresponds to a Y^+ of order 10 or less. The surface grid spacings at the rotor leading and trailing edges and the stator trailing edge are less than about 0.18 mm (0.007 in).

Method of Analysis

The following procedure was followed to achieve a turbine stage solution. Preliminary stator-only and rotor-only solutions were obtained. These blade row solutions, which modeled the blade rows as independent of each other, were then combined and information was passed between them iteratively until a converged stage solution was reached.

For the preliminary blade row calculations, the same grids were used as in the final calculations. The stator-only computation was conducted with the inlet total pressure and temperature from the experiment applied as upstream boundary conditions. Additionally, zero swirl velocity was assumed upstream of the stator since velocities are very low there (Mach 0.05 or less), and the flow is entering radially from a large volute. It was impossible to calculate the flow through the stator alone using the entire streamwise grid, since conservation of angular momentum and the absence of a rotor to extract energy would result in a physically impossible solution. Therefore the stator-only calculation was limited to the region upstream of the rotor leading edge. The experimental inter-blade row hub static pressure was employed as the exit boundary condition. This was 179 KPa (26.0 psi), or 53.5% of the upstream total pressure. Spanwise equilibrium (axial) was applied at the exit boundary. The solution was initialized using a very simple axisymmetric starting solution based on constant total conditions and velocity magnitudes through the machine and meridional flow tangency to the meridional grid lines. This estimate neglects increases in swirl through the stator, but proved adequate as a starting solution.

The rotor-only solution utilized the entire rotor grid, and applied the same total temperature as the stator-only solution at the upstream boundary. The total pressure at the inlet boundary was reduced to 98% of the experimental stator inlet total pressure to account for the stator losses. The exit boundary condition was the experimental rotor exit static pressure at the hub (44.6 KPa (6.46 psi), or 13.3% of the experimental stator inlet total pressure), and radial equilibrium was applied at the exit boundary. The rotor speed was fixed at the experimental value. Inlet swirl was varied until the flow angle at the radial location of the stator trailing edge approximately equalled the stator trailing edge blade angle of 73 degrees. This was later found to overestimate the final stage calculation of the stator exit angle by about 3 degrees. However, for a preliminary solution, small errors such as this are not a major concern. As in the stator-only solution, the rotor-only solution was started with an estimate based on constant total conditions and velocity magnitudes through the machine and meridional flow tangency to meridional grid lines. This was again found to be adequate. The rotor-only solution converged to a mass flow rate less than 2% greater than the stator-only solution.

A converged stage solution using the average passage code is achieved by alternating between calculations on each blade row. During a given blade row calculation, a set of axisymmetric body forces are applied which model the effects of the absent blade row. Although the body forces are axisymmetric, the flow retains its three-dimensionality throughout the domain due to the presence of the current blade row. The body forces effect changes in the six flow variables (density, three components of momentum per unit volume, energy per unit volume, and pressure) at each solution point by additive adjustments calculated from the previous calculation on the absent blade row. Since the three-dimensional grids are not axisymmetric, it is necessary for the code to interpolate the body forces, as well as the axisymmetric flow solution, from one blade row calculation to the other when a new blade row is started.

It proved difficult to achieve a converged stage solution using the preliminary stator and rotor solutions with the experimental boundary conditions. Using a procedure of alternating between 100 iterations on each blade row, while restarting each blade row with its previous solution yielded divergent mass flow rates for the stator and rotor. This was likely due to the highly sensitive nature of the transonic flow between the blade rows to flow rate, and its resulting effect on rotor incidence. As the mass flow rate fluctuated, the rotor incidence deviated from the design incidence angle. This caused the flow in the inter-blade row space to fluctuate even more, resulting in instability. After careful examination of the problem, a new solution methodology was attempted which resulted in a converged solution. The rotor-only solution was recalculated using the total temperature, entropy, and tangential and axial velocity components at the stator exit from the stator-only axisymmetric solution as inflow boundary conditions. The rotor-only calculation was then executed, holding the hub exit pressure constant, but varying the rotor speed until the flow rate through the rotor equalled the stator-only value. This required an increase in the design rotor speed of about 2%. Using this new rotor speed, stator and rotor solutions were again alternated with 100 iterations on each blade row. Before restarting each new rotor solution, an axisymmetric correction was added to the previous rotor solution in the stator space to make the axisymmetric solution in that space equal to the current stator axisymmetric solution. A comparable procedure was followed for each new stator solution. This improved convergence by ensuring compatibility between the body forces and the axisymmetric solution in the absent blade row space. The two axisymmetric solutions approach each other as the solution converges. After this stage calculation converged, the rotor speed was gradually reduced to the experimental value. This calculation methodology ensures that mass flow rates in the two calculations are always equal, thus avoiding the problems encountered previously. The stage calculation was considered converged when the flow rate had reached a constant value for several cycles between stator and rotor, and the root-mean-square residual of each blade row had decreased by at least three orders of magnitude from the original starting solutions. The residual was defined as the time derivative of the circumferential momentum per unit volume at a solution point.

To help understand the relative merit of the stage solution, a three-dimensional isolated rotor solution was computed having the same mass-averaged absolute total pressure and mass-averaged circumferential momentum as the stage calculation midway between blade rows. Fixing these quantities allows the mass flow to vary, which is consistent with the stage calculation methodology. The

upstream boundary was located upstream of the stator. The circumferential momentum was produced by imparting the necessary swirl at the upstream boundary. The stage rotor solution was used as the starting solution for this calculation. All pertinent calculation variables were held constant from the stage calculation. The root-mean-square residual of this solution was brought to a lower value than that of the stage solution. It may be argued that the axisymmetric flow profile should be fixed to the correct spanwise distribution immediately upstream of the rotor, but this would introduce loss due to the interaction of rotor potential effects with this new upstream boundary.

The computations were performed on the NASA Lewis and Ames Cray Y-MP supercomputers. The stage solution required approximately 5000 iterations to reach a converged solution, not including aborted attempts at achieving convergence. This corresponds to approximately 10 CPU hours of Cray Y-MP time. The computational grid, executable code, and flow solution required about 12 megawords of combined memory. The supplemental isolated rotor solution required approximately an additional 1000 iterations from the stage rotor solution, corresponding to approximately 1.3 CPU hours of Cray Y-MP time.

Results and Discussion

The final converged stage calculation predicts a mass flow rate through the turbine of 2.93 kg/s (6.46 lb/s), while the isolated rotor solution yields a mass flow rate of 2.76 kg/s (6.09 lb/s). These values are approximately 2.6% above and 3.3% below the experimental value of 2.86 kg/s (6.30 lb/s), respectively. The high mass flow predicted by the stage calculation can possibly be explained by geometric differences between the computational grid and the actual rig hardware. Because of machining tolerances, it is possible that the actual flow area of the turbine differed slightly from the computational grid, which matched the design coordinates. This is critical for the stator, where a slight change in the large exit angle can effect a large change in throughflow. The initial stator-only solution mass flow rate was comparable to the final stage mass flow, which was higher than the experimental value. This stator-only mass flow was rather insensitive to pressure ratio, indicating that the stator was near a choked condition. In the isolated rotor solution, the stator blades are not present, and the mass flow rate is 3.3% below the experimental value, despite the fact that the mass-averaged absolute total pressure between blade rows is matched to the stage calculation. This is due to the thicker endwall boundary layers which form in the absence of stator blades. Because of the slowing at the endwalls, the core flow has more swirl than the stage calculation, since the mass-averaged circumferential momentum is the same. This causes a spanwise variation in flow angle between blade rows, compared to the nearly spanwise uniform stage calculation flow angle, and an associated reduction in flow rate.

Figures 7 and 8 present Mach number contours relative to each blade row at midspan for the stator and rotor passages, respectively, from the stage calculation. Flow is from top to bottom in both figures. Wakes can be seen downstream of both blades, although they diffuse in a rather short distance. The very low Mach number upstream of the stator (less than 0.05) can be seen in Fig. 7. This very slow flow presents a convergence problem for compressible schemes such as the one used in this study. However, through the use of increased levels of artificial dissipation in the early stages of the calculation, these problems were circumvented. A small

region of high velocity flow can be seen in the rotor solution (Fig. 8) near the suction surface downstream of the leading edge. This region is caused by the positive incidence calculated by the code and the resultant acceleration of the flow around the blade leading edge. This high velocity flow is decelerated by the viscous drag at the blade and the slower flow in the mid-passage, before re-accelerating through the rotor. The solution does not predict any flow separation due to the deceleration. The rotor geometry of this analysis has a truly radial leading edge. The second rotor designed and fabricated by Pratt and Whitney has a leaned leading edge, such that the blade is not radial at the leading edge. This lean would tend to align the blade with the incident flow, perhaps eliminating the accelerated region and reducing incidence loss.
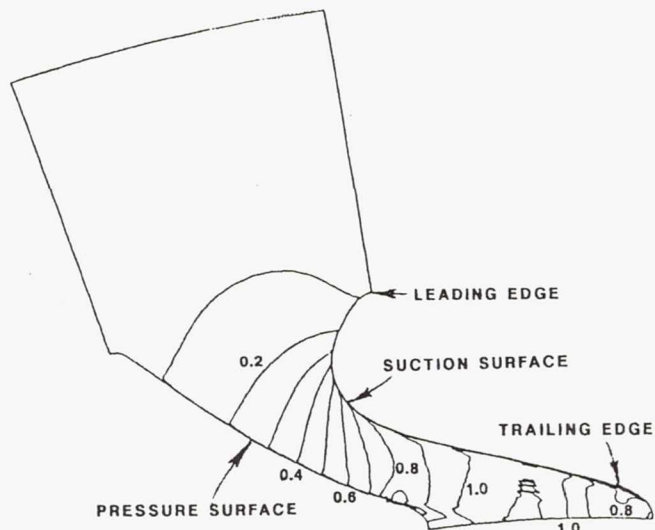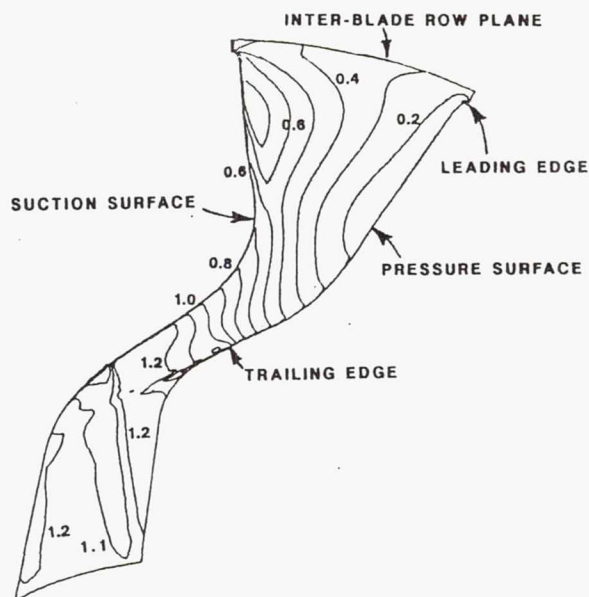

Figure 7. Stator midspan Mach number

Figure 8. Rotor midspan relative Mach number

Figures 9 and 10 display total pressure contours between blade rows for the experiment and stage calculation, respectively, viewed from downstream. The experimental plot is for the second stator configuration, where the blades have been rotated by 1.125 degrees relative to the calculation. However, it is anticipated that the distribution of loss will not vary dramatically due to this rotation. The stator wake can clearly be seen in both plots and is comparable. The low total pressure endwall vortices span a greater circumferential distance in the experiment than in the calculation. This discrepancy may be due to the inability to match the stepwise change in span between blade rows with the computational grid. The smooth grid may allow the vortices to remain localized. It is curious that the experimental data is not symmetric about the midspan in Figure 9. Since the stator geometry and inflow are symmetric and the stator is near a choked condition, a symmetric profile such as that seen in Figure 10 is expected.
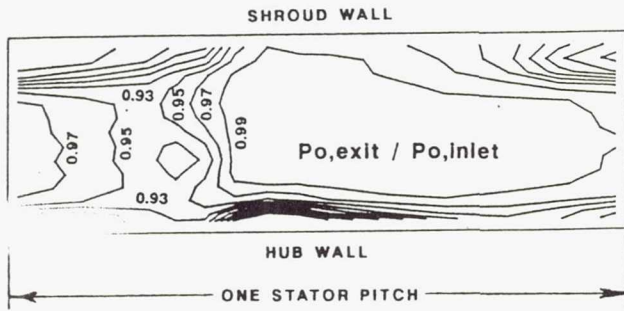

Figure 11. Stator loading diagram

Figure 9. Experimental stator exit total pressure contours viewed from downstream

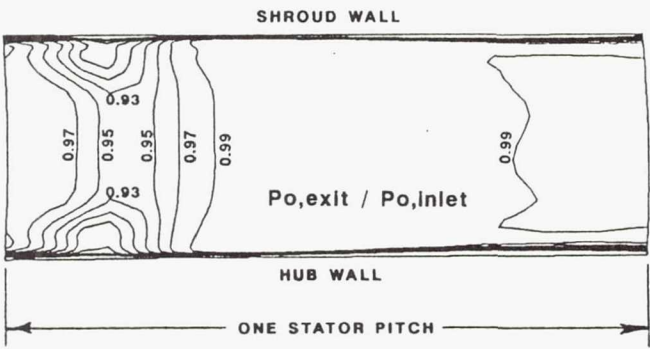Figure 12. Stage rotor loading diagram

Figure 10. Calculated stator exit total pressure contours viewed from downstream

Loading diagrams for the stator and rotor from the stage calculation and for the rotor from the isolated rotor calculation are presented in Figs. 11, 12, and 13, respectively. The surface pressures are normalized by the stator inlet total pressure. Spans are measured from the hub. The 10%, 50%, and 90% span locations were chosen to represent hub, midspan, and tip values while avoiding highly localized effects near the rotor
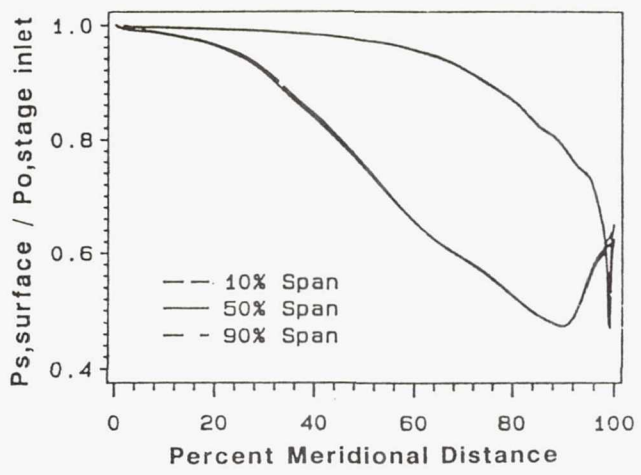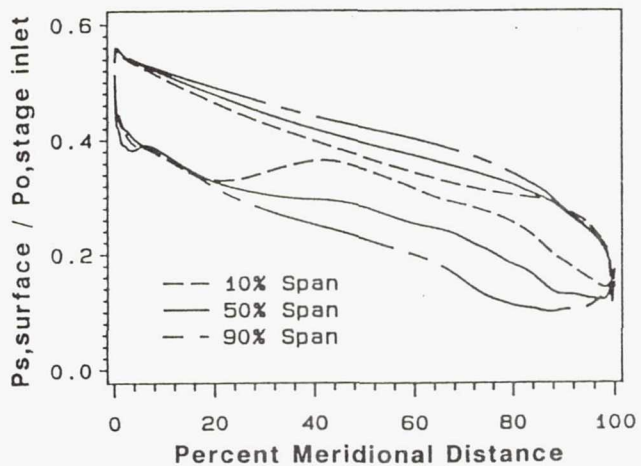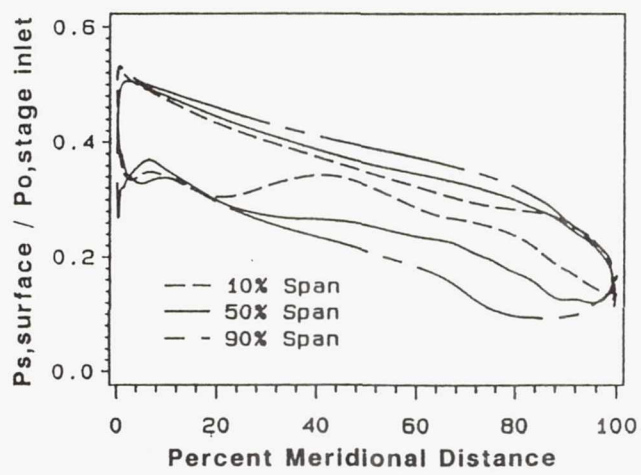

Figure 13. Isolated rotor loading diagram

clearances. The stator loading is nearly spanwise constant, with only slight differences near the endwalls. The 10% and 90% span loadings are identical, indicating symmetry about midspan. The stator is mainly loaded over the rear half of the blade, where the higher velocities occur. The rotor stage solution loading diagram (Fig. 12) indicates approximately constant spanwise loading in the radial part of the rotor (0 to 30 percent meridional distance), and radially increasing loading in the mixed and axial regions (30 to 100 percent meridional distance). In the radial part of the rotor, the flow is still nearly two-dimensional because a cross-channel slice is at constant radius, thus the loading is two-dimensional. As the rotor turns toward the axial direction, more work is extracted from the flow at the larger radii due to the larger blade-to-blade distance, resulting in larger pressure differences across the blade. The isolated rotor solution loading diagram (Fig. 13) is quite similar to the rotor stage solution loading diagram. However, the blade surface pressures are consistently lower for the isolated rotor solution. This is due to a lower relative total pressure between blade rows in the isolated rotor solution which occurs despite the matching of absolute total pressure. The isolated rotor solution also indicates a lower loading at 50% span than near the endwalls in the rotor leading edge region. This is a result of the spanwise variation in mass flow rate caused by the thicker stator endwall boundary layers in the isolated rotor solution. While the tangential and total velocities are largest at midspan, the throughflow velocity is actually largest at about 10% and 90% span. This results in higher loading at these locations. This is unrealistic and points out the superiority of the stage calculation.

Figures 14 and 15 show relative velocity vectors near the hub and suction surfaces for the stator and rotor stage solutions, respectively. The stator flow (Fig. 14) is nearly two-dimensional, which is supported by Figs. 9 and 10. There is no apparent separation, and losses result almost completely from skin friction. In the rotor (Fig. 15), low momentum fluid migrates from hub to shroud along the suction surface, sweeping the boundary layer flow toward the blade tip, where the clearance flow detaches it from the blade and carries it into the passage. The radial flow migration is driven by hub and suction surface pressure gradients which are illustrated in Fig. 12. A pressure surface pressure gradient, although smaller, also exists and drives the flow in the opposite direction (radially inward). The circumferential arc on the hub in Fig. 15 indicates the junction of the rotating disk and the stationary backface. The rotation of the backface and shroud relative to the rotor is right to left, and viscous drag pulls the boundary layer fluid toward the blade suction surface. The hub and tip clearance flows oppose this viscous flow. There is no apparent flow separation on the rotor walls.

The net result of the various flow phenomena which take place in the rotor is illustrated in the axial component of vorticity (rigid body angular velocity) distribution at the blade trailing edge plane (Fig. 16). The formation of the turbulent wake is seen along the blade trailing edges. The positive (counterclockwise) axial vorticity in the wake is consistent with the upward migration of fluid on the suction surface and the downward migration on the pressure surface. When particles were released near the hub trailing edge using a three-dimensional plotting program, they migrated slowly along the trailing edge from hub to tip. This is due to centrifugal forces acting upon the very low momentum fluid in the center of the small trailing edge
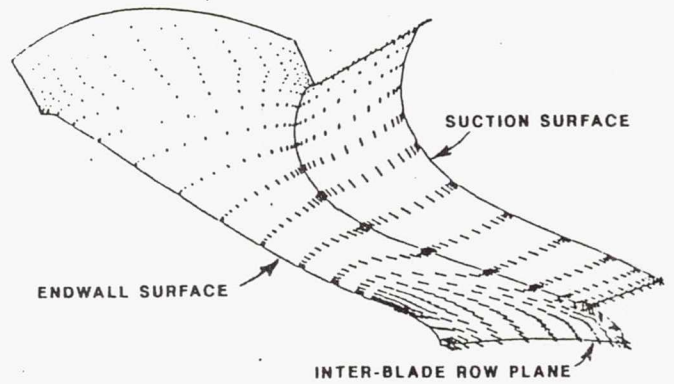

Figure 14. Velocity vectors near stator endwall and suction surfaces
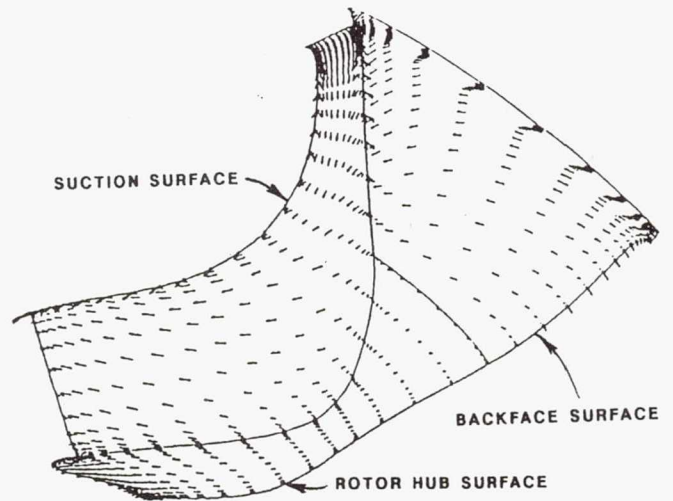

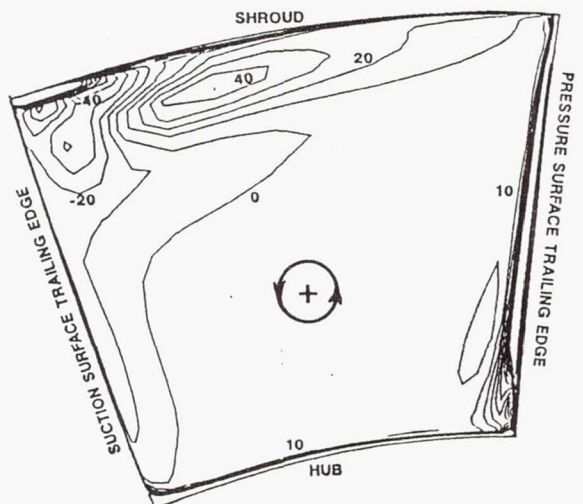Figure 15. Relative velocity vectors near rotor hub and suction surfaces

Figure 16. Rotor trailing edge axial vorticity

8

vortices which result from trailing edge separation. The negative (clockwise) vortex near the shroud/suction surface corner is caused by the tip leakage flow which is from left to right. It is essentially an extension of the larger area of negative vorticity near the suction surface caused by the spanwise migration of suction surface flow. Squeezed between the tip leakage vortex and the shroud is a very thin, very intense positive (counterclockwise) vortex which is a result of viscous drag at the shroud from right to left. The larger and more diffuse positive vortex near mid-channel and 90% span is also caused by the shroud drag, but is limited by the leakage flow to some distance from the suction surface. This vortex is similar to the vortex found in the driven cavity problem.

Figure 17 indicates the effect of the aforementioned secondary flows on turbine loss through entropy contours at the trailing edge plane. The highest entropy regions are in the wake and at the tip leakage discharge. As stated previously, the blade suction surface boundary layer flow migrates toward the tip where the tip leakage flow detaches it from the blade and carries it into the passage. This is substantiated by the high entropy region emanating from the clearance region into the passage in Fig. 17. This high entropy flow is forced away from the shroud as it moves toward the pressure surface by the larger positive vortex of Fig. 16. Particles were released into the flow backwards in time from the center of the high entropy region using a three-dimensional plotting program. This was done to determine the origin of this high loss flow. The particles were found to originate from the tip clearance region at about 30% meridional distance. This does not suggest that all of the loss originates there, but merely substantiates the premise that the tip clearance flow plays an important role in producing and distributing the loss.
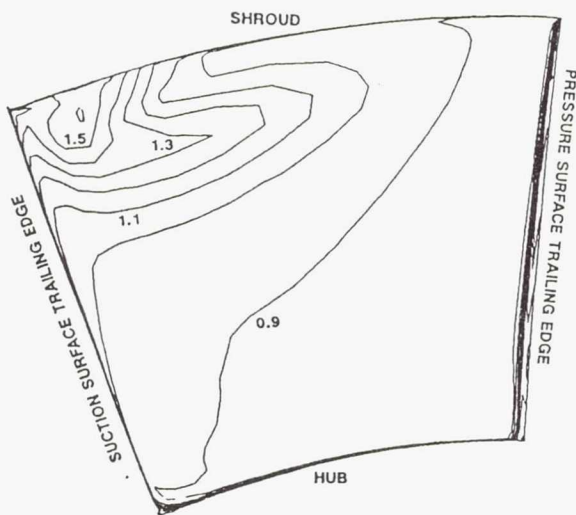

Figure 17. Rotor trailing edge entropy

Figures 18 to 21 compare axisymmetric area-averaged computational results downstream of the rotor with experimental data. The area average was used because it is arguably what steady-state probes measure in an experimental setting. These plots also include the isolated rotor solution for comparison, and are taken at the outflow boundary of the solution, which corresponds to the data measuring station. Figure 18 shows the axisymmetric rotor exit flow angle distribution versus

percent span, where zero percent span indicates the hub. Both stage and isolated rotor solutions are presented. Negative flow angles indicate a tangential component of absolute velocity opposite to the direction of rotation of the rotor. It is interesting that the two calculations agree so well with each other in light of the fact that they have quite different inflow conditions. This indicates that the rotor exit flow angle distribution is driven mostly by the rotor, and that the distribution of stator exit angle has a relatively small effect. Of course if the circumferential momentum upstream of the rotor were not the same for the two cases, one would expect the average exit flow angles for the two cases to differ. The agreement with experimental data is quite good, especially between 10% and 90% span. The location of the local maxima at 75% span is predicted accurately. The deviation of the calculations from the data near the endwalls is difficult to explain. However, there is only one data point at each endwall which is not predicted, and they are very close to the endwalls. Because the boundary layer flow is slow at the endwalls, a small change in swirl velocity would result in a large change in flow angle compared to the higher velocity flow in the core. Thus the misprediction of swirl velocity at the endwalls is actually not very large.
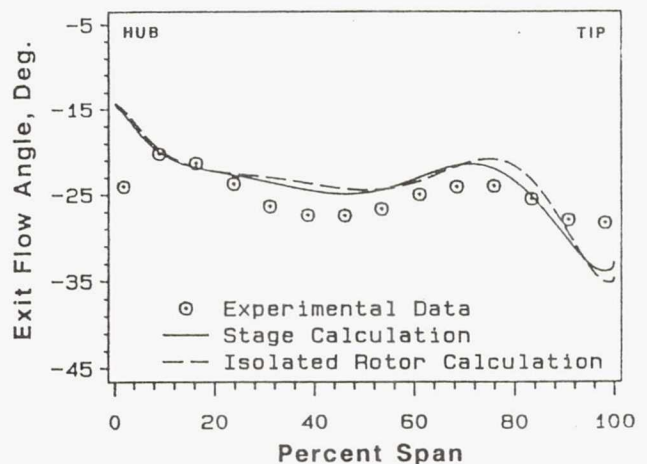

Figure 18. Axisymmetric absolute flow angle downstream of rotor

Figure 19 presents the total pressure distribution at the rotor exit. The pressures are normalized by the stator inlet total pressure. In an integrated sense, the stage calculation overpredicts the exit total pressure slightly, while the isolated rotor calculation underpredicts it by about the same amount. The lower exit total pressure for the isolated rotor calculation is consistent with the lower static pressures found on the blade surfaces in Fig. 13 than in Fig. 12, and is caused by the lower relative total pressure between blade rows in this solution. The two calculations have nearly the same distribution of rotor exit total pressure, which matches that of the data well except for the small peak in the data near 70% span. This difference becomes more apparent in the following two figures.

Figure 20 is a plot of rotor exit total temperature versus percent span. The values are normalized by the stator inlet total temperature. Exit total temperature is an indication of the amount of work done by the fluid. A lower exit total temperature indicates more work.
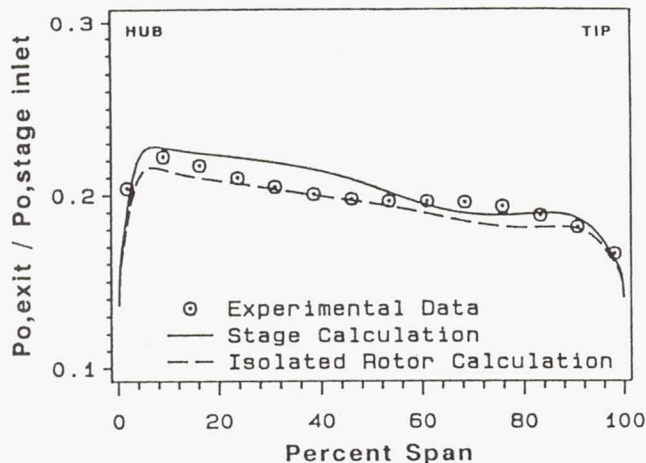
Figure 19. Axisymmetric total pressure
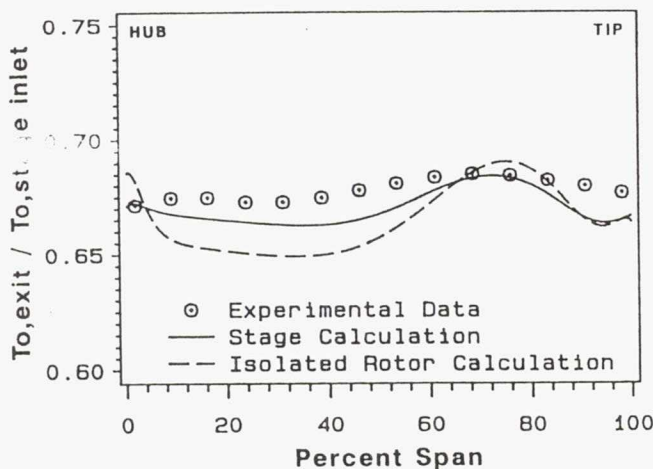downstream of rotor

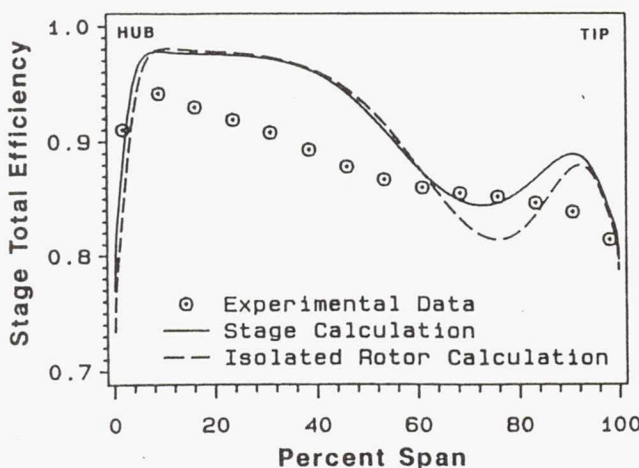Figure 20. Axisymmetric total temperature
downstream of rotor

Figure 21. Axisymmetric efficiency
downstream of rotor

Figure 20 indicates a higher level of work done in the isolated rotor calculation than in the stage calculation. This is consistent with the total pressure distributions of Fig. 19. The isolated rotor calculation predicts a lower rotor exit total pressure than the stage calculation. This corresponds to a higher total pressure ratio across the stage, and a higher ideal change in total enthalpy. Thus for a comparable efficiency, the isolated rotor calculation should predict a higher actual change in total enthalpy with a resulting lower exit total temperature. Between 10% and 50% span, the isolated rotor exit total temperature is consistently lower than the stage prediction, in agreement with the exit total pressure trends. Near 70% span, however, both calculations predict an increase in rotor exit total temperature. This increase corresponds in location to the local maxima of the experimental data near 70% span, but the magnitude of the variation is larger in the calculations. This is especially true for the isolated rotor calculation, where the work done is significantly lower near 75% span. The increased exit total temperature near the hub in the isolated rotor solution is likely due to the increased loss associated with the thicker hub boundary layer which forms in the stator space in the absence of stator blades. This effect may also be responsible for part of the increase near the shroud. It is expected that the effect of the endwall boundary layer would be more diffuse near the shroud due to the mixing effect of the tip clearance flow.

Figure 21 presents the stage total-to-total efficiency distributions at the rotor exit. The mass-averaged efficiency for the experiment is 88%, while the stage and isolated rotor calculations predict mass-averaged efficiencies of 91% and 90%, respectively. The two calculations are essentially identical except between 65% and 95% span. Over this range, the isolated rotor calculation exhibits a more dramatic reduction in efficiency. Figures 16 and 17 help explain the cause of the calculated reduction in efficiency near 75% span. The high entropy region near the suction surface trailing edge at 90% span migrates to about 75% span at the downstream exit plane due to the effect of the larger positive (counterclockwise) vortex of Fig. 16. This high loss region is a result of the accumulation of boundary layer and clearance flow through the rotor. The isolated rotor solution has more rotor inlet loss concentrated at the endwalls. Much of the hub endwall flow migrates from hub to tip on the rotor suction surface, while much of the shroud endwall flow is driven to the tip clearance by shroud relative rotation. In this way the additional endwall loss in the isolated rotor solution supplements the high entropy region at the rotor exit, yielding a larger reduction in efficiency at 75% span. The efficiency trend is thus superior for the stage calculation compared to the isolated rotor solution, because the experimental data shows no such local minimum in efficiency. It is unclear why the calculations predict a minimum at 75% span while the data is monotonically decreasing through this range. Perhaps the tip clearance loss is distributed more equally across the span than predicted. This is supported by the overprediction of efficiency between 10% and 50% span. The rather simple inviscid clearance model may cause the leakage jet to diffuse more slowly than in reality, retaining the localization of the loss. It would be desirable to have experimental data closer to the rotor trailing edge to determine whether the efficiency distribution has more spanwise variation nearer the rotor.

Summary and Conclusions

The compact radial turbine stage flow field was analyzed with the three-dimensional Navier-Stokes average passage code. This code calculates the flow through a blade row using axisymmetric body forces to model the effects of the absent blade row. The solution was compared with experimental stator and rotor exit quantities and with a corresponding calculation of the flow through the isolated rotor. The stage calculation produced somewhat better agreement with experimental data in terms of the spanwise distribution of rotor exit quantities. The calculation also produces results not measured in the experimental study and some of these, including stator and rotor loading diagrams, rotor exit vorticity and entropy contours, and surface velocity vectors are presented to better describe the complex flow field in the turbine stage. The isolated rotor calculation was found to be unrealistic due to the formation of thick endwall boundary layers in the vacated stator space which are not present in the stage calculation because of the stator blades. These endwall boundary layers result in unrealistically large spanwise variations of the flow quantities entering the rotor, while the stage calculation predicts the expected nearly spanwise constant rotor inlet flow. The spanwise variations of the isolated rotor solution give rise to an unrealistic loading diagram near the rotor leading edge, an enthalpy change through the rotor larger and having more spanwise variation than that found experimentally, and a reduction in efficiency at 75% span which is more extreme than either the stage calculation or experiment.

While the use of three-dimensional Navier-Stokes codes has grown for turbomachinery analysis purposes, the application of these codes to the design of turbomachinery has been limited by the computational time required to achieve a solution. This paper makes no claim toward solving this problem. However, this analysis does improve the modeling of a single stage radial turbine by more accurately accounting for the effect of the upstream stator blades. The improved modeling brings improved agreement with experimental data. This improved agreement, in concert with the ability of three-dimensional Navier-Stokes codes to track loss production and distribution through turbomachinery, could give a designer new information to improve future turbomachinery designs.

Acknowledgements

References

1. Choo, Y. K. and Civinskas, K. C., "Three-Dimensional Inviscid Analysis of Radial Turbine Flow and a Limited Comparison With Experimental Data", NASA TM No. 87091, 1985 and USAAVSCOM Technical Report 85-C-12.

2. Denton, J. D., "A Method of Calculating Fully Three-Dimensional Inviscid Flow Through Any Type of Turbomachine Blade Row", Aerothermodynamics of Low Pressure Steam Turbines and Condensers, Vol. 1, VKI-LS-1983-06-VOL-1, Von Karman Institute for Fluid Dynamics, Rhode-Saint-Genese, Belgium, 1983.

3. Zangeneh-Kazemi, M., Dawes, W. N. and Hawthorne, W. R., "Three Dimensional Flow in Radial Turbines", ASME Paper No. 88-GT-103.

4. Heidmann, J. D. and Beach, T. A., "An Analysis of the Viscous Flow Through a Compact Radial Turbine by the Average Passage Approach", NASA TM No. 102471, June, 1990 and ASME Paper No. 90-GT-64.

5. Moore, J. and Moore, J. G., "Calculations of Three-Dimensional Viscous Flow and Wake Development in a Centrifugal Impeller", Journal of Engineering for Power, Volume 103, pp. 367-372, April, 1981.

6. Rhie, C. M., Delaney, R. A., and McKain, T. F., "Three-Dimensional Viscous Flow Analysis for Centrifugal Impellers", AIAA-84-1296, June 1984.

7. Dawes, W. N., "Towards Improved Throughflow Capability: The Use of 3D Viscous Flow Solvers in a Multistage Environment", ASME Paper No. 90-GT-18.

8. Denton, J. D., "The Calculation of Three Dimensional Viscous Flow Through Multistage Turbomachines", ASME Paper No. 90-GT-19.

9. Adamczyk, J. J., "Model Equation for Simulating Flows in Multistage Turbomachinery", NASA TM No. 86869, November, 1984 and ASME Paper No. 85-GT-226.

10. Adamczyk, J. J., Mulac, R. A. and Celestina, M. L., "A Model for Closing the Inviscid Form of the Average-Passage Equation System", ASME Paper No. 86-GT-227.

11. Celestina, M. L., Mulac, R. A. and Adamczyk, J. J., "A Numerical Simulation of the Inviscid Flow Through a Counterrotating Propeller", Journal of Turbomachinery, Volume 108, pp. 187-193, October, 1986.

12. Fredmonski, A. J., Huber, F., Simonyi, P. S., and Roelke, R. J., "Design and Experimental Evaluation of a Compact Radial-Inflow Turbine", AIAA-91-2127, June 1991.

13. Simonyi, P.S. and Boyle, R. J., "Comparison of Analysis and Experimental Performance for Three Compact Radial Turbines", AIAA-91-2128, June 1991.

14. Jameson, A., Schmidt, W., and Turkel, E., "Numerical Solutions of the Euler Equations by Finite Volume Methods Using Runge-Kutta Time-Stepping Schemes", AIAA-81-1259, June 1981.

15. Beach, T. A., "An Interactive Grid Generation Procedure for Axial and Radial Flow Turbomachinery", NASA Contractor Report 185167, November 1989 and AIAA-90-0344.

Report Documentation Page

1. Report No. NASA TM – 104420	2. Government Accession No.	3. Recipient's Catalog No.

4. Title and Subtitle A Three-Dimensional Navier-Stokes Stage Analysis of the Flow Through a Compact Radial Turbine		5. Report Date
		6. Performing Organization Code

7. Author(s) James D. Heidmann	8. Performing Organization Report No. E – 6254
	10. Work Unit No. 505 – 05 – 10

9. Performing Organization Name and Address National Aeronautics and Space Administration Lewis Research Center Cleveland, Ohio 44135 – 3191	11. Contract or Grant No.
	13. Type of Report and Period Covered Technical Memorandum

12. Sponsoring Agency Name and Address National Aeronautics and Space Administration Washington, D.C. 20546 – 0001	
	14. Sponsoring Agency Code

16. Abstract

A steady, three-dimensional Navier-Stokes "average passage" computer code is used to analyze the flow through a compact radial turbine stage. The code is based upon the average passage set of equations for turbomachinery, whereby the flow fields for all passages in a given blade row are assumed to be identical while retaining their three-dimensionality. A stage solution is achieved by alternating between stator and rotor calculations, while coupling the two solutions by means of a set of axisymmetric body forces which model the absent blade row. Results from the stage calculation are compared with experimental data and with results from an isolated rotor solution having axisymmetric inlet flow quantities upstream of the vacated stator space. Although the mass-averaged loss through the rotor is comparable for both solutions, the details of the loss distribution differ due to stator effects. The stage calculation predicts smaller spanwise variations in efficiency, in closer agreement with the data. The results of this study indicate that stage analyses such as this hold promise for improved prediction of loss mechanisms in multi-blade row turbomachinery, which could lead to improved designs through the reduction of these losses.

17. Key Words (Suggested by Author(s)) Turbines Navier-Stokes equation Radial flow	18. Distribution Statement Unclassified - Unlimited Subject Category 07

19. Security Classif. (of the report) Unclassified	20. Security Classif. (of this page) Unclassified	21. No. of pages 12	22. Price* A03

National Aeronautics and
Space Administration

Lewis Research Center
Cleveland, Ohio 44135

Official Business
Penalty for Private Use $300

FOURTH CLASS MAIL

ADDRESS CORRECTION REQUESTED

||||||

U.S.MAIL

Postage and Fees Paid
National Aeronautics and
Space Administration
NASA 451

NASA